
Simplify
your imaging workflows

ADVANCED FUNCTIONAL MATERIALS
www.afm-journal.de

A Rational Design for a High-Safety Lithium-Ion Battery Assembled with a Heatproof–Fireproof Bifunctional Separator

Longqing Peng, Xiangbang Kong, Hang Li, Xin Wang, Chuan Shi, Texiong Hu, Yizhen Liu, Peng Zhang, and Jinbao Zhao**

High-Ni-content $LiNi_xCo_yMn_{1-x-y}O_2$ is regarded as a feasible cathode material to meet the urgent requirement for high energy density batteries. However, such cathode has a poor safety performance because of reactive oxygen releasing at elevated temperatures. In pursuit of high-safety lithium-ion batteries, a heatproof–fireproof bifunctional separator is designed in this study by coating ammonium polyphosphate (APP) particles on a ceramic-coated separator modified with phenol-formaldehyde resin (CCS@PFR). The CCS@PFR separator acts as a thermal-supporting layer to inhibit the shrinkage of the separator at elevated temperatures, whereas the APP-coated layer functions as a fireproof layer, forming a dense polyphosphoric acid (PPA) layer above 300 °C. The PPA layer not only isolates the combustibles from the highly reactive oxygen released from the cathodes but also converts violent combustion reactions into mild stepwise exothermic reactions by carbonizing the combustibles in the batteries. Enabled with such a heatproof–fireproof bifunctional separator, $LiNi_{0.8}Co_{0.1}Mn_{0.1}O_2|SiO_x$–Gr full cells are constructed and these exhibit an excellent safety performance by not catching fire during a 30 s combustion test and surviving the 10 min high-temperature test above 300 °C. Additionally, an adiabatic rate calorimeter and nail penetration test are conducted with 3 Ah $LiNi_{0.8}Co_{0.1}Mn_{0.1}O_2|SiO_x$–Gr pouch cells to further verify the safety performance.

1. Introduction

Owing to their high energy density and long cycle life, lithium-ion batteries (LIBs) play a vital role in our daily lives.[1] They are the ideal power source for portable electronic devices, such as mobile phones and laptops, and are expected to become one of the main power sources for electric vehicles. However, with the increasing demand for higher energy density, the LIB safety concerns become so serious that they frustrate the development of clean and efficient energy utilization. Solutions to the safety problems are urgently required for the application of LIBs with a high energy density.[2]

Thermal runaway is one of the main reasons for the safety issues in LIBs. Once the heat generation rate is higher than its dissipation rate, heat will accumulate and induce an increase in temperature, causing more drastic exothermic side reactions, and finally resulting in the thermal runaway of LIBs.[3] Although the mechanism of thermal runaway of LIBs is still controversial, it can be divided into three stages. The first stage is the original heat accumulation below 120 °C in which the accumulation of the heat released during the battery operation or the external heat leads to the decomposition and regeneration of the solid electrolyte interphase, which then drives the temperature up to the next stage. In the second stage, an internal short-circuit occurs because of the shrinkage of the separator at ≈130–150 °C, which consequently leads to a sharp rise in the cell temperature up to the third stage above 200 °C. In the last stage, the cathode begins to release highly reactive oxygen species, which further leads to the severe redox reaction of the combustible materials in batteries, eventually resulting in the thermal runaway of LIBs.[2b,4]

The most severe safety issue that might cause casualties is often associated with the third stage, the drastic burning of combustible materials in the LIBs, which generates large amounts of gas and heat, leading to a rapid growth in pressure. Consequently, the battery violently explodes, further accelerating the spread of the flame. Hence, inhibiting the burning of LIBs is critical to avoid major disasters. There are three necessary requisites for the occurrence of combustion,

L. Peng, X. Kong, H. Li, X. Wang, Prof. J. Zhao
College of Chemistry and Chemical Engineering
Xiamen University
Engineering Research Center of Electrochemical Technology
Ministry of Education
State-Province Joint Engineering Laboratory of Power Source
Xiamen University
Xiamen 361005, China
E-mail: jbzhao@xmu.edu.cn

Prof. C. Shi
College of Physics
Qingdao University
Qingdao 266071, China

T. Hu, Y. Liu, Prof. P. Zhang, Prof. J. Zhao
College of Energy Research and School of Energy Research
Xiamen University
Xiamen 361102, China
E-mail: pengzhang@xmu.edu.cn

The ORCID identification number(s) for the author(s) of this article can be found under https://doi.org/10.1002/adfm.202008537.

DOI: 10.1002/adfm.202008537

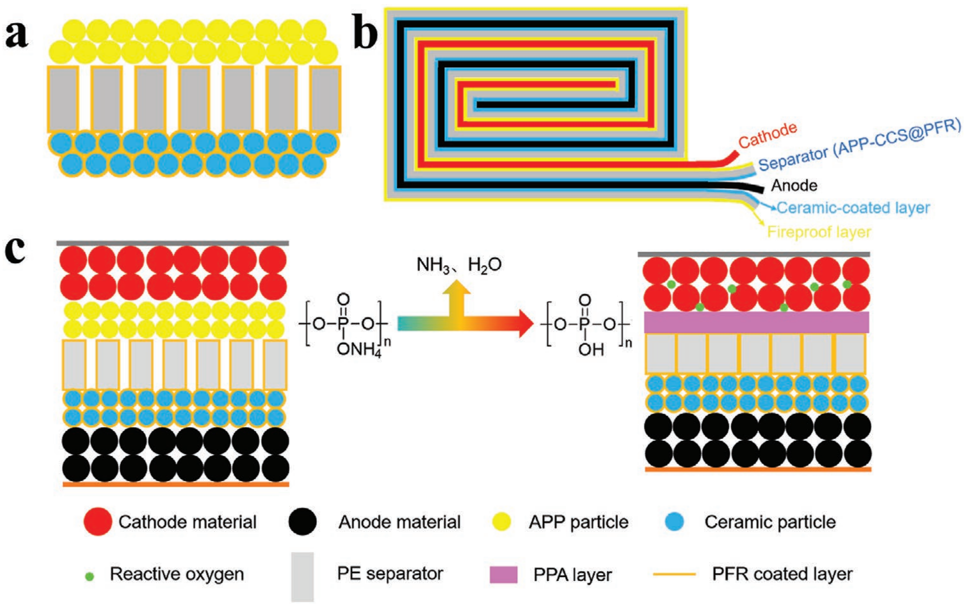

Figure 1. a) The APP-CCS@PFR schematic; b) structure of high-safety LIBs assembled with APP-CCS@PFR; and c) safety mechanism of APP-CCS@PFR for LIBs.

including the presence of combustibles, the coexistence of oxidants (usually oxygen in air), and a temperature that is above the ignition point. On this basis, there are three strategies to address the burning issue of LIBs. The first one is to substitute the combustion liquid electrolyte with a nonflammable liquid electrolyte or solid-state electrolyte; however, the use of a nonflammable liquid electrolyte compromises the performance of the LIBs,[5] and the commercial application of a solid-state electrolyte is still in its infancy.[6] The second strategy is to maintain the temperature of the cell below the ignition point of the combustibles; in practice, a battery management system (BMS) is deployed, which activates the cooling circulation system or the radiator fan when the temperature is too high. Nevertheless, limited by the heat dissipation capacity of the BMS, heat cannot be effectively dissipated in time when thermal runaway occurs in abuse situations. The last strategy is to separate the combustibles and oxidants. It is worth noting that the oxidants, during the thermal runaway process of LIBs, not only originate from oxygen in the air but also originate from the phase transition or the decomposition of cathodes at high temperature.[7] Therefore, to prevent the burning of LIBs, oxidants from both origins should be addressed.

In line with this issue, phosphoric flame retardants have been widely used in various materials, such as cloth, coating, and engineering plastic because of its advantages of a high flame retardant efficiency, environment-friendliness, and low cost,.[8] According to their working principles, phosphoric flame retardants are classified into three categories, namely, free-radical-quenching flame retardants (FRQFRs), endothermal-cooling flame retardants (ECFRs), and physical-isolation flame retardants. However, FRQFRs and ECFRs are not suitable for LIBs because the addition of a large amount of flame retardants to the supporting electrolyte decreases the ionic conductivity and significantly deteriorates the electrochemical performance of LIBs.[9] In this study, ammonium polyphosphate (APP), which could serve as a flame retardant by the physical isolation mechanism, was selected to modify our separator. At temperatures above 300 °C, APP decomposes, forming a dense polyphosphoric acid (PPA) layer, which acts as a barrier to isolate the combustibles from the highly reactive oxygen released from the cathode.

However, limited by the poor thermal stability of the polyolefin separator, the separator modified with only APP particles will suffer from severe shrinkage at elevated temperatures, and this will not only expose the combustibles to the oxidants but also cause an internal short-circuit at elevated temperatures. Inspired by our previous studies,[3a,10] herein a phenol-formaldehyde-resin (PFR)-modified ceramic-coated separator (CCS@PFR), which exhibits an excellent thermal dimension stability (exhibiting no visible shrinkage up to 300 °C), was employed as a substrate separator. A layer of APP particles was coated onto the uncoated side of the CCS@PFR separator to yield a heatproof–fireproof bifunctional separator APP-CCS@PFR, as shown in **Figure 1**a. Using such a bifunctional separator, a high-safety battery was constructed by orienting the fireproof-coated layer of APP-CCS@PFR to the cathode side and outer layer of the cell, as shown in Figure 1b. The safety mechanism of APP-CCS@PFR for LIBs is shown in Figure 1c. On the one hand, the CCS@PFR substrate separator, as a 3D thermally stable supporting membrane, could avoid the separator-shrinkage-caused internal short-circuit because of the second-stage thermal runaway. On the other hand, the APP fireproof coating layer forms a dense PPA protective layer, effectively cutting off contact between the combustibles and the oxidants, originating from the external air or the cathode in the third stage of thermal runaway, thus preventing the occurrence of battery burning. Consequently, the thus-constructed cell exhibited an excellent safety performance by surviving a series of harsh safety tests.

2. Results and Discussion

2.1. Morphology and Composition Characterization

Separators require a constantly flat and even surface. Failure to achieve this leads to poor contact with the electrodes, resulting in a significant impact on the ionic flux and the electrochemical performance of LIBs.[11] Furthermore, to increase the energy density of LIBs, the separator should be as thin as possible, while not compromising the safety of LIBs. However, the pristine commercial APP particles, whose diameters are ≈5–10 µm (Figure S1a, Supporting Information), are too large to form a smooth and thin coating layer on the surface of the substrate separator. Therefore, mechanical ball milling was applied to pulverize the APP particles into smaller particles, as specified in detail in Figure S1b–d (Supporting Information). The APP was pulverized into uniform and fine particles, as shown in Figure S1d (Supporting Information). Figure S2 (Supporting Information) shows that the Fourier transform infrared (FTIR) spectrum of APP after mechanical ball milling was consistent with that of the pristine commercial APP particles, demonstrating that the APP particles did not undergo a chemical change in the ball-milling process. Figure S3 (Supporting Information) shows that milling reduced the average size of the APP particles from ≈6.8 to 1.2 µm. The scanning electron microscopy (SEM) image presented in **Figure 2**a reveals a smooth and porous coating layer on the CCS@PFR surface, confirming the structural integrity of the APP-coated layer. Cross-sectional SEM images (Figure 2b–d) clearly confirmed a 5 µm thick APP coating layer (Figure 2c) and a 3 µm thick ceramic coating layer (Figure 2d) on the two sides of the PE separator. Energy-dispersive X-ray (EDX) elemental mapping was conducted to further determine the elemental composition of each layer. As depicted in Figure 2e–h, the distributions of C and Al correspond to the area of the PE separator and the ceramic coating layer, respectively; P is associated with the APP coating layer and O was observed on both sides of the separator, further confirming the presence of the APP coating layer and the ceramic coating layer on each side.

Figures S4 and S5 (Supporting Information) present the thermogravimetric analysis (TGA) of APP under an argon atmosphere and the relevant decomposition products, respectively. Thermal degradation processes can be mainly divided into two steps, the initial weight loss from 288 to 549 °C corresponded to the release of NH_3 and H_2O during the formation of highly crosslinked PPA and the second weight loss beyond 549 °C corresponded to the release of phosphoric acid, metaphosphoric acid, or some partially crosslinked PPA molecules.[12]

2.2. Thermal Dimensional Stability of APP-Modified Separator

Although the thermal stability of separators could not fully prevent LIBs from runaway, it is still an essential requirement for the safety of LIBs. Many reports on separators with high thermal stability have been published in recent years.[13] However, the most commonly used separators are still based on microporous polyolefin separators, owing to the overall consideration of mechanical strength, production efficiency, cost, thermal shut-down function, and electrochemical performance. It is still the most practical and effective way to modify polyolefin separators to improve their thermal stability and electrolyte wettability.[3a,14] Atomic layer deposition (ALD) technology has been applied to improve the performance of separators, owing to its ability to form an ultrathin and conformal layer with an accurate and controlled thickness. Lee et al. reported a multilayer separator with an ultrathin 5 nm Al_2O_3 layer through a novel roll-to-roll atmospheric ALD technology, which showed excellent flexibility, high conformity, suppressed thermal shrinkage, high electrolyte wettability, and improved tensile strength.[15] Despite these advantages, the relatively low productivity and high cost, as compared to ceramic-coated separators, may limit its commercial application.

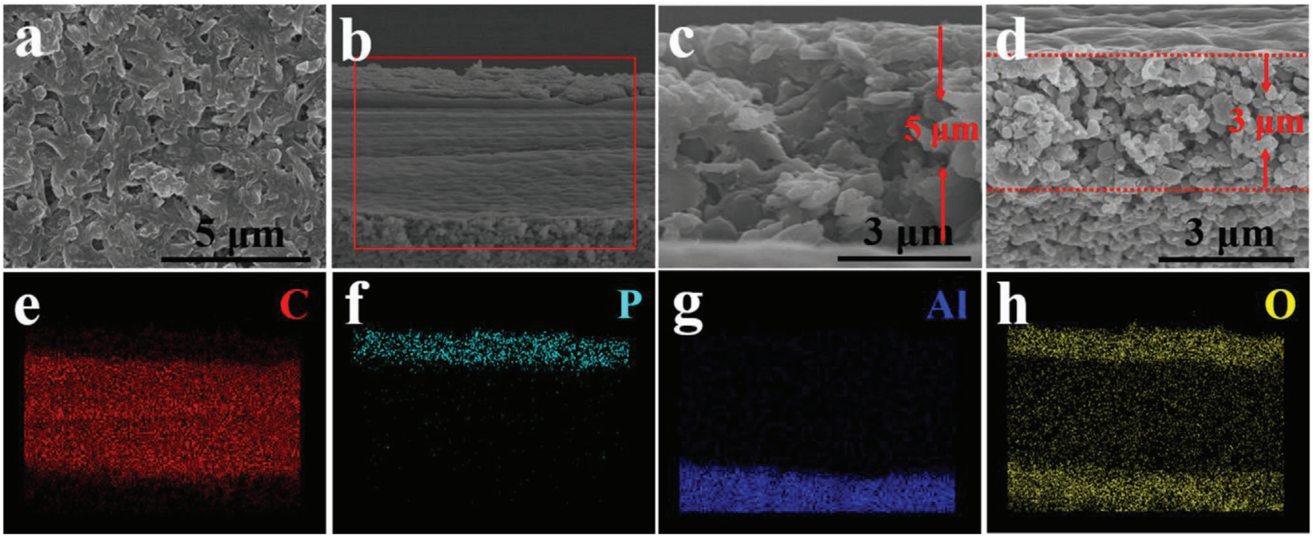

Figure 2. a) An APP-coated layer SEM image; b) cross-sectional SEM image of APP-CCS@PFR; c,d) enlarged cross-sectional SEM images of the APP-coated layer and the ceramic-coated layer, respectively; and e–h) EDX elemental mapping of C, P, Al, and O, respectively, for the area represented by the red square in (b).

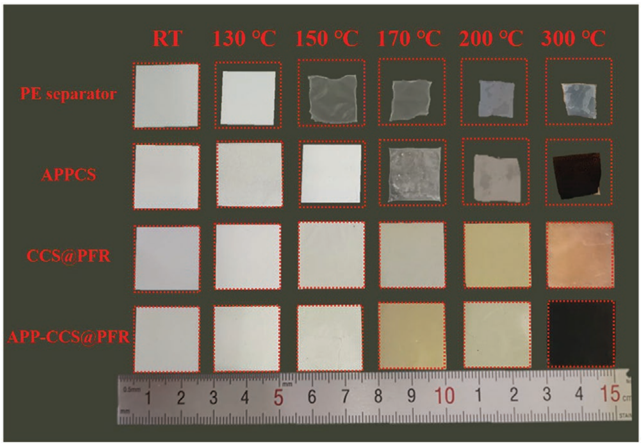

Figure 3. Photographs of the PE, APPCS,CCS@PFR, and APP-CCS@PFR separators after the thermal shrinkage test at various temperatures for 30 min.

Herein, our high thermal stability CCS@PFR separator, which was prepared by further modifying single-side ceramic-coated separator with a 3D PFR-coated layer throughout the entire separator, was chosen as a substrate separator. APP-CCS@PFR was obtained by modifying APP particles on the uncoated side of the CCS@PFR. Thermal shrinkage tests at various temperatures were conducted to evaluate the thermal stability of the separators. As shown in **Figure 3**, the PE separator exhibited a shrinkage of 38.8% at 130 °C and became transparent with a larger shrinkage of 59.6%, 71.2%, and 77.5% at 150, 170, and 200 °C, respectively. APP modification enhanced the thermal dimensional stability by demonstrating no visible shrinkage at 130 °C. Although APP exhibited a thermal stability of up to 288 °C, the weak interaction between APP particles does not resist the shrinkage of the PE separator when the binder melts or softens at elevated temperatures. The separator, with only coated APP particles on one side of the PE separator (APPCS) still exhibited shrinkages of 13.5%, 36.2%, and 51.1% at 150, 170, and 200 °C, respectively. CCS@PFR exhibited no visible shrinkage up to 300 °C. This result was consistent with our previous report.[10] This is because PFR formed a 3D coating layer throughout the entire substrate separator and connected the ceramic-coated layer and PE separator as a whole. Therefore, it enhanced the adhesion, strength, and toughness of the ceramic-coated layer, preventing the ceramic-coated layer from shrinking with the PE separator. Owing to the high thermal stability of CCS@PFR, it is evident that APP-CCS@PFR, a modified CCS@PFR separator with APP particles, also exhibited excellent thermal stability, which made it possible for the APP-coated layer to form a dense overall-covered layer to protect the LIBs from thermal runaway at elevated temperatures. Additionally, APPCS and APP-CCS@PFR became black after heat treatment at 300 °C, owing to the generation of PPA, further carbonizing the polyolefin separator in the char layer, which contains P—O—C structures and aromatic species.[16] Figure S6 (Supporting Information) presents the APPCS FTIR spectra after the heat shrinkage test at 300 °C. The broad band between 1150 and 1300 cm^{-1} was attributed to the P—O—C bond,[16c] and the absorption peak at 1601 cm^{-1} indicated the generation of aromatic species. It is worth noting that the formation of the char layer was because of the PPA forcing the reorganization of the polyethylene skeleton carbon atoms into C=C or P—O—C. Therefore, the char layer mainly forms in the PE layer. The ceramic-coated layer remains electronically insulated to prevent the internal short-circuit of the cell. Additionally, it has been reported that a modified separator with a partially electronically conductive coating layer mitigates the impact of internal shorting by increasing the internal short-circuit resistance.[17] Therefore, even if the char layer may partially cause electronic shorting of the cell at elevated temperatures, it could not cause the severe thermal runaway of LIBs. The char layer acts as a physical barrier to the transport of heat, combustible gas, and oxygen, thereby forming an isolation layer between the combustibles and oxygen and effectively preventing the battery from catching fire.[12a,18]

2.3. Combustion and High-Temperature Full-Cell Tests

Owing to their higher energy density, $LiNi_{0.8}Co_{0.1}Mn_{0.1}O_2|SiO_x$-Gr batteries are supposed to achieve the 300 Wh kg^{-1} target for LIBs.[4c,19] However, except for the intrinsic poor safety performance of $LiNi_{0.8}Co_{0.1}Mn_{0.1}O_2$ cathode materials, the faster capacity fading of the SiO_x-Gr anode aggravated the safety performance because the decreased capacity ratio of the negative electrode to the positive electrode may cause overcharging of the cell and precipitation of lithium metal on the anode.[20] Therefore, $LiNi_{0.8}Co_{0.1}Mn_{0.1}O_2|SiO_x$-Gr full batteries were assembled to verify the safety performance of APP-CCS@PFR. After activation, the cells were charged to 4.3 V at 0.5 C, and the outer aluminum plastic films were removed for subsequent combustion tests. As shown in **Figure 4**a, the cell assembled

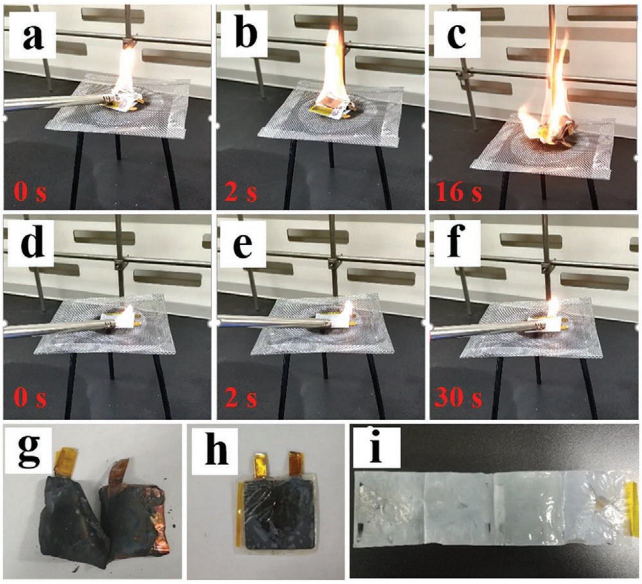

Figure 4. The combustion test of $LiNi_{0.8}Co_{0.1}Mn_{0.1}O_2|SiO_x$-Gr full cells assembled with a a–c) PE separator and d–f) APP-CCS@PFR at various times after ignition, respectively. g,h) Photographs of the cell assembled with a PE separator and APP-CCS@PFR after the combustion test, respectively. i) Photograph of APP-CCS@PFR after the combustion test.

with the PE separator immediately caught fire when exposed to a flame and kept on burning even after the flame source was removed (Figure 4b). As the fire progressed, it further led to the thermal runaway of the battery and intensified the burning of the cell (Figure 4c), resulting in a burnt-out battery without a visible separator and electrolyte (Figure 4g). The cell assembled with APP-CCS@PFR could not be ignited even after continuous combustion for 30 s, as shown in Figure 4d–f. The cell remained intact after the combustion test, as shown in Figure 4h. The APP-CCS@PFR after the test only exhibited minor wrinkling without any visible dimensional shrinkage (Figure 4i). Figure S7a (Supporting Information) presents the SEM image of the APP-CCS@PFR after the combustion. The micropores in the APP-coated layer disappeared and a dense layer covered the surface of the separator. Furthermore, EDX elemental analysis was conducted to determine the composition of the dense layer. Figure S7b (Supporting Information) shows that the C, N, O, F, and P elemental contents were 0.02, 0.01, 25.98, 37.87 and 36.12 wt%, respectively. The F element originated from the $LiPF_6$ in the electrolyte. The disappearance of N demonstrated the release of NH_3 combined with the generation of PPA. This corresponds with the TGA and FTIR results of APP after heating. The absence of the C signal indicates that the electrolyte was volatilized or covered by the dense PPA layer. It is worth noting that the test time was only 30 s, which was insufficient for the diffusion of PPA or heat to carbonize the PE separator. There was little evidence of carbon in the EDX result of the separator after the combustion test. Additionally, the attenuated total reflection infrared spectrum of the APP-coated side of the APP-CCS@PFR separator after the combustion test was acquired. Figure S8 (Supporting Information) shows that the surface of the APP-coated layer after the combustion test contained all the characteristic absorption bands of PPA at 2843, 2350, 1648, 1220, and 989 cm^{-1}, further verifying that the major component of the dense covering layer was PPA.

The combustion test results showed that APP can form a dense PPA layer at high temperatures, preventing contact of the combustibles and oxygen in the air, thereby avoiding the burning of the battery. However, this is not sufficient to ensure the safety of the batteries, especially for $LiNi_xCo_yMn_{1-x-y}O_2$ and $LiCoO_2$ cathode materials, because the cathodes release highly reactive oxygen at high temperatures and cause severe redox reactions of the combustible materials inside the batteries.[7b]

To further verify that the APP-coated layer can effectively prevent the burning of LIBs from the highly reactive oxygen released from cathodes at high temperatures, four types of cells with different structures were assembled for the high-temperature test. The cells were charged and pretreated as in the combustion test. **Figure 5**a–d depicts the simplified configurations of the four types of cells, and the images of cells during and after the test are provided under the configurations, respectively. Figure 5a shows that the cell assembled with the PE separator caught fire after 5 s in a muffle furnace above 300 °C, and finally burns out with a fractured cell. Figure 5b shows the result of the cell assembled with CCS@PFR. Despite

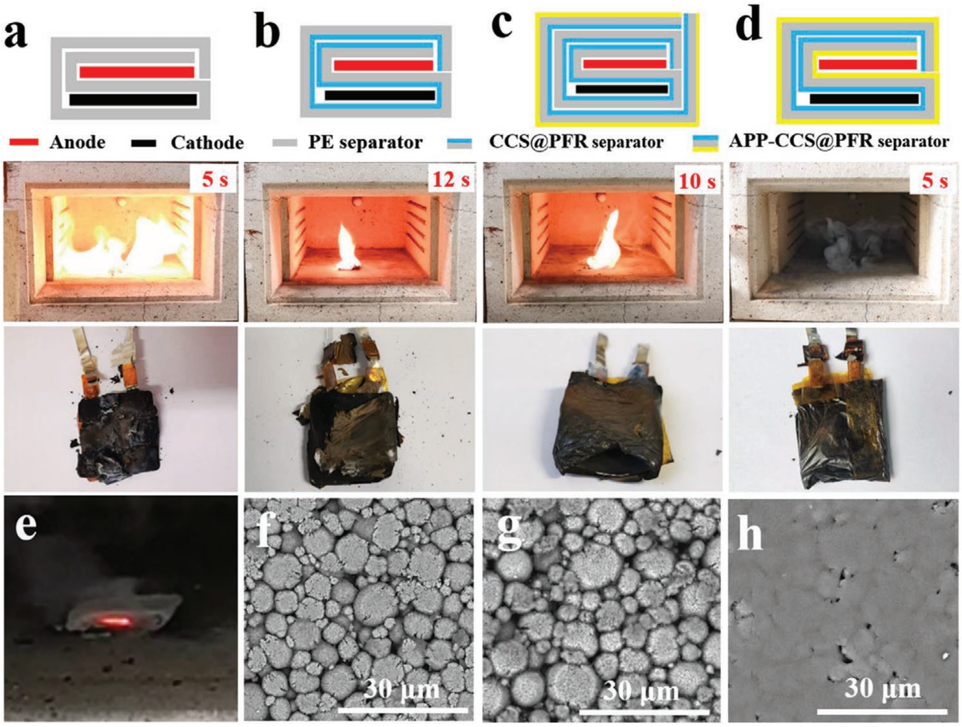

Figure 5. Models of the four cell types for the high-temperature tests. The images of the cells during and after the test are shown under the configurations, respectively. a–d) The colors correspond to the schematic shown in Figure 1, namely, red (cathode), black (anode), blue (ceramic-coated layer), yellow (fireproof layer), and gray (PE separator), respectively; e) image of the cell assembled with CCS@PFR and further packaged with APP-CCS@PFR when it caught fire; f) image of the original cathode; and g,h) the cathode of the cells assembled with CCS@PFR and APP-CCS@PFR after the high-temperature test, respectively.

the excellent thermal stability, the cell assembled with CCS@PFR also caught fire after 12 s and a ceramic-coated layer remained on the surface of the electrodes. Figure 5c shows the cell assembled with CCS@PFR and further packaged with APP-CCS@PFR. Although the outer APP-CCS@PFR separator could form a dense layer to prevent contact between the combustibles and external oxygen, the cell also ignited after a 10 s exposure. The outer APP-CCS@PFR packing layer maintained its dimensional integrity after the test, whereas the cell swelled and exposed the internal electrodes. The fire originated inside the battery, as shown in Figure 5e, and the battery expanded between the cathode and separator. The results demonstrated that a fireproof layer only on the outer surface of the cell was not sufficient to guarantee the safety of LIBs, because the highly reactive oxygen released from the cathode will also cause the severe redox reaction of the combustible materials, and ultimately lead to the burning of the cell. It is worth noting that the results in Figure 5a–c also demonstrated that the use of a high thermal stability separator delayed the runaway to some extent, and the flame of the cell assembled with CCS@PFR was milder than that assembled with the PE separator. The cell assembled with APP-CCS@PFR only exhibited wisps of smoke without a flame after the cell was placed in the muffle furnace above 300 °C (Figure 5d) for 5 s. The smoke disappeared after several seconds, and no thermal runaway was observed within the following 10 min. As shown in Figure 5d, although the separator was carbonized after 10 min of high-temperature treatment, it still maintained its dimensional stability and wrapped the entire battery inside to avoid the contact of combustibles with oxidants.

2.4. Mechanism for Preventing the Burning of LIBs

SEM images of the original cathode (Figure 5f) and the cathodes of the cells assembled with CCS@PFR (Figure 5g) and APP-CCS@PFR (Figure 5h) after testing were obtained to further understand the mechanism of APP for preventing the burning of the cell. The morphology of the cathode of the cell assembled with CCS@PFR showed no distinct change after the test, whereas a dense layer was clearly formed on the cathode surface of the cell assembled with APP-CCS@PFR. For more details, EDX elemental analysis was conducted to determine the composition of the covering layer. Figure S9 (Supporting Information) shows that the content of the N, O, P, Ni, Co, and Mn elements are 0.73, 37.49, 43.11, 13.50, 2.29, and 1.03 wt%, respectively. The contents of N and P elements were similar to the results of the EDX elemental analysis after the combustible test, which demonstrated the release of NH_3 with the generation of PPA. To acquire more details of the posthumous materials after the high-temperature test, a Leica EM TIC 3X was used to prepare cross-sectional samples of the cathodes after the high-temperature test. **Figure 6**a,b shows that the cathode surface of the cell assembled with APP-CCS@PFR (Figure 6b) appeared as a 1–3 μm covering layer after the high-temperature test. Figure 6c–f presents the EDX elemental mapping for Figure 6b. O was distributed in both the covering layer and the cathode particles, whereas P and Ni were mainly distributed in the covering layer and the cathode particles, respectively. The distribution of F in the cavities between the cathode particles originated from the binder and $LiPF_6$ or their decomposition products at elevated temperatures. Table S3 (Supporting Information) presents the element content analysis for Figure 6b and demonstrates the disappearance of N after the high-temperature test. Therefore, the result further verified that the major component of the covering layer was PPA. Figure S10 (Supporting Information) shows the SEM images of APP-CCS@PFR after the test. The granular APP particles of the APP-coated layer disappeared with a dense covered layer. The ceramic-coated layer maintained a smooth and compact surface morphology without cracks, which acted as an isolation layer to restrain the transfer of heat, combustible gas, and oxygen, thereby protecting the cell from catching fire.

Differential scanning calorimetry (DSC) and TGA tests of the PE separator, APPCS, and APP-CCS@PFR at a heating rate of 5 °C min^{-1} under a purified air atmosphere were also conducted. **Figure 7** shows that the PE separator suffered a violent combustion reaction at 406.3 °C with a tremendous maximum heat flow value of 30.3 mW mg^{-1}. The decomposition of the APPCS and APP-CCS@PFR separators was split into three much milder exothermic peaks with maximum heat flow values of only 4.35 and 3.04 mW mg^{-1}, respectively. The first exothermic process may be because of the partial oxidation of the PE separator, leading to a slight increase in mass because of the absorption of O, as shown in the enlarged inset of Figure 7. It was clear that APPCS and APP-CCS@PFR had higher heat flow values than the PE separator at ≈200–260 °C. This may be because the porous structure and the inherent polarity of the APP-coated layer captured more oxygen, which promoted the oxidation of the PE membrane. However, the oxidation of the PE separator was still quite moderate and was insufficient to cause the thermal runaway of the LIBs and was beneficial to homogenize the exothermic process. The second process at 300–400 °C corresponded to the carbonization of the separator by the PPA generated from the decomposition of APP.[16b,21] PPA prompted the reorganization of carbon atoms into a dense char layer containing P—O—C structures and aromatic species, thereby indirectly restraining the oxidation of the C—H and C—C groups.[16b,c] The consequent product of the dense char layer restrained the transfer of heat, combustible gas, and oxygen. Therefore it delayed the decomposition of the PE separator from 406 to 424.2 and 428.4 °C for APPCS and APP-CCS@PFR, respectively. The intensity of the decomposition reaction was also largely suppressed because of the isolation effect of the char layer and the stepwise exothermic process. The mass residual rates of the PE separator, APPCS, and APP-CCS@PFR were 0%, 22.9%, and 45.6%, respectively, after the TGA test at 800 °C. Additionally, the char residual rates of APPCS and APP-CCS@PFR were ≈10.9% and 11.2%, as calculated by subtracting the mass residual rates of other compositions shown in Tables S1 and S2 (Supporting Information).

Therefore, the possible mechanism of APP for preventing the burning of LIBs can be explained as follows. As shown in **Figure 8**, APP decomposed into NH_3, H_2O, and PPA at high temperatures. NH_3 and H_2O diluted the concentration of combustible gas and oxygen to some extent, and the generation of PPA covered the surfaces of the cathode and cell, isolating the combustibles from the oxidants in the air and cathode.

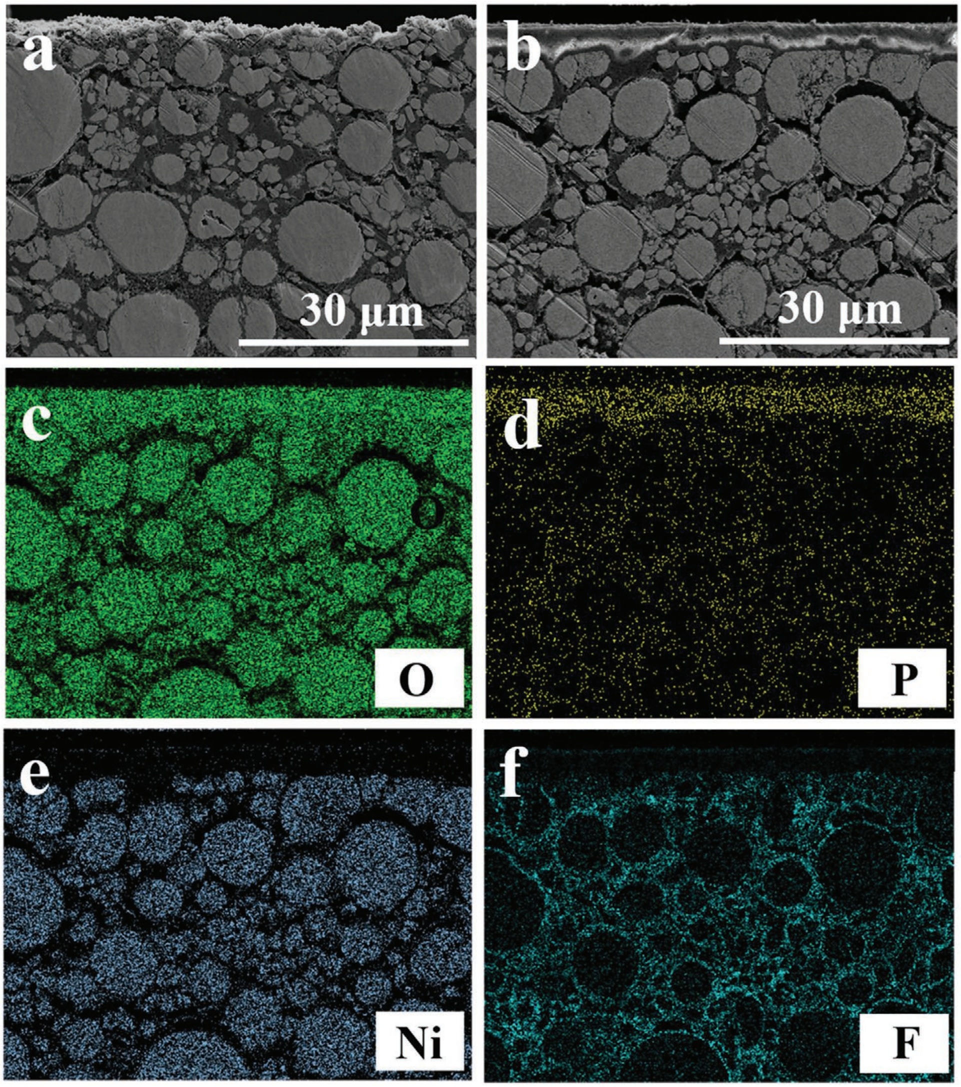

Figure 6. a,b) Cross-sectional SEM image of the cathodes of the cell assembled with CCS@PFR and APP-CCS@PFR, respectively, after the high-temperature test. c–f) The EDX elemental mapping of O, P, Ni, and F for (b).

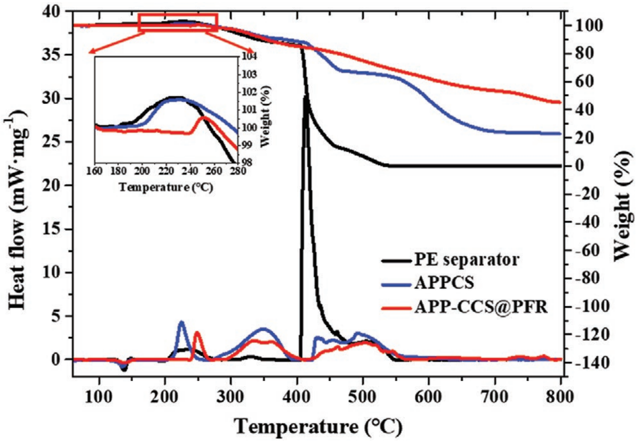

Figure 7. The DSC and TGA results of the PE separator, APPCS, and APP-CCS@PFR at a heating rate of 5 °C min^{-1} under a purified air atmosphere.

Subsequently, PPA further carbonized the combustibles, such as the electrolyte and separator, into nonflammable char residues, which converted the violent and rapid combustion reaction into a mild and prolonged exothermic reaction. Additionally, the dense char residue layer restrained the transfer of heat, combustible gas, and oxygen, thereby protecting the LIBs from catching fire.[12a,18]

2.5. Safety Tests with 3Ah Pouch Cells

Accelerating rate calorimetry (ARC) analysis is an important safety test for LIBs for practical applications. The cells were heated at 5 °C per step under adiabatic conditions. If the self-heating rate was less than the set value during the 20 min monitoring process, the cells are heated to the next temperature step. If not, the cells will start self-heating, and the temperature is recorded. **Figure 9**a,b shows the ARC test results

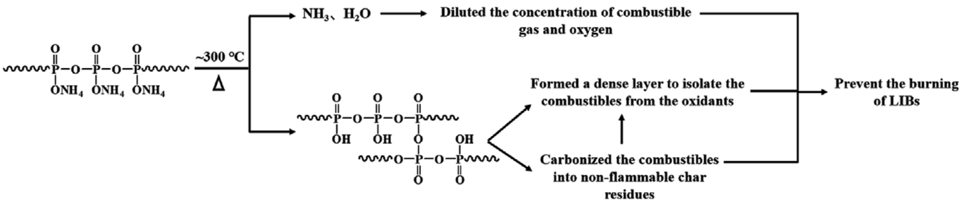

Figure 8. The APP mechanism for preventing the burning of LIBs.

of 3 Ah $LiNi_{0.8}Co_{0.1}Mn_{0.1}O_2|SiO_x$-Gr full cells assembled with CCS@PFR and APP-CCS@PFR, respectively. The cell assembled with CCS@PFR started self-heating at ≈80.1 °C and a violent thermal runaway ensued with a maximum temperature exceeding 450 °C. However, the cell assembled with APP-CCS@PFR cooled down after a slow self-heating process without a violent thermal runaway. Figure 9c–f presents photographs of the cells after the test was concluded. The cell assembled with CCS@PFR suffered from a drastic thermal runaway with a burned aluminium-plastic film and fragmented electrodes (Figure 9c,d). The cell assembled with APP-CCS@PFR swelled into a big package without visible thermal runaway, and the electrodes and separators remained nearly intact after the test (Figure 9e,f).

The nail penetration test is regarded as the most demanding safety test for LIBs, especially for LIBs with high energy density cathode materials. During the nail penetration test, a steel nail is driven into the cell, and the cathodes and anodes are partially connected with each other inside the cell by the electron conducting nail, which results in an abrupt internal short-circuit at the interface of the nail and electrodes. A large amount of joule heat is thus generated owing to the high short-circuit current. Excessive heat increases the temperature of the cell and further leads to a series of exothermic side reactions and aggravates the

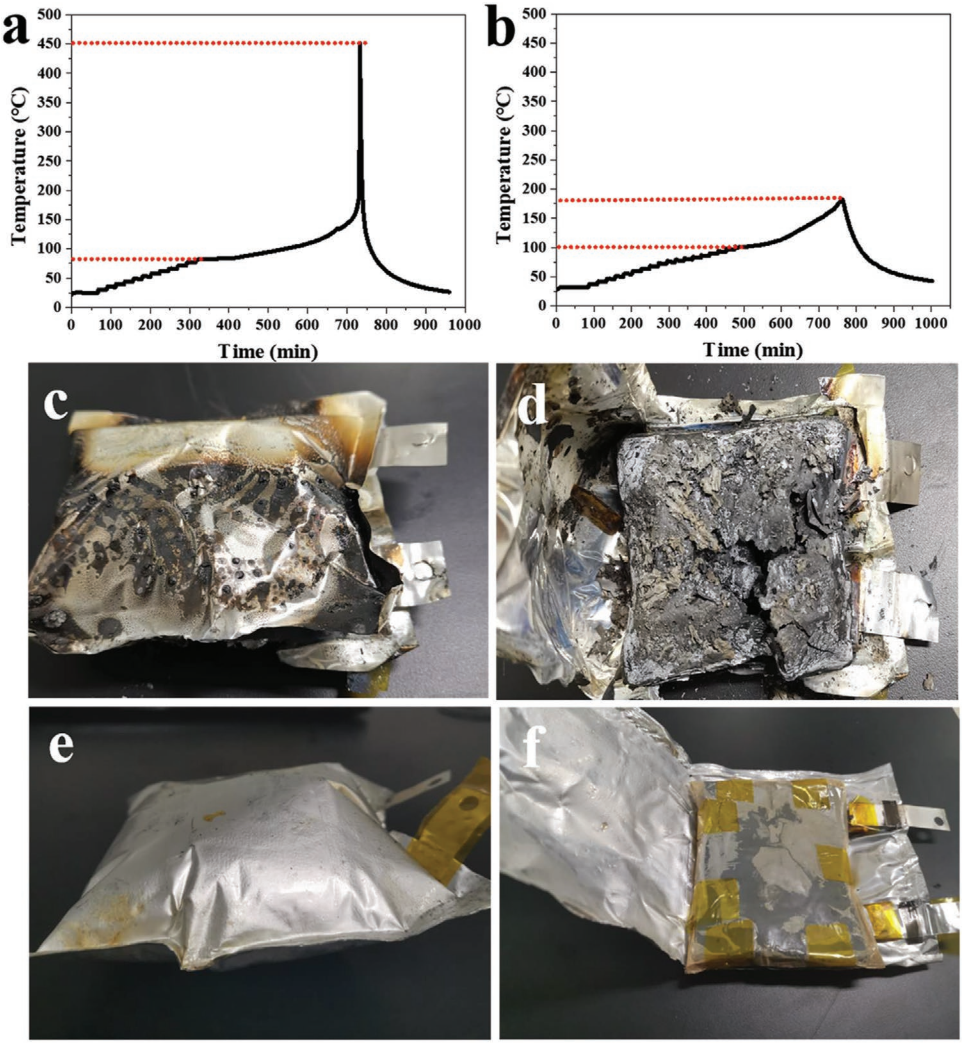

Figure 9. a,b) The ARC test results of the cells assembled with the CCS@PFR and APP-CCS@PFR, respectively. Photographs of the batteries assembled with the CCS@PFR (c,d) and APP-CCS@PFR (e,f) after the ARC test.

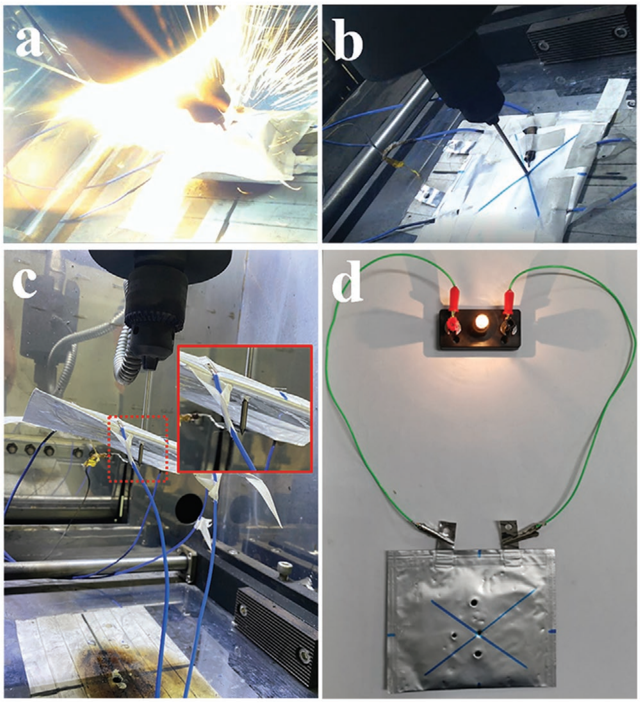

Figure 10. a,b) Photographs of the nail penetration test of the batteries assembled with CCS@PFR and APP-CCS@PFR, respectively. Photographs of the cell assembled with APP-CCS@PFR c) after testing and d) the cell lighting a bulb.

shrinkage of the separator. If no current shutdown is effective, the temperature will upsurge to out of control and result in the thermal runaway of the LIB.

Nail penetration tests of the 3 Ah $LiNi_{0.8}Co_{0.1}Mn_{0.1}O_2|SiO_x$-Gr cells assembled with CCS@PFR and APP-CCS@PFR were conducted to investigate the function of the APP-coated layer to improve the safety performance of LIBs. **Figure 10**a shows that the cell assembled with CCS@PFR immediately broke out into a violent flame when the steel nail penetrated the cell. However, no visible thermal runaway was observed during the nail penetration test of the cell assembled with APP-CCS@PFR (Figure 10b). Figure 10c shows the needle perforating through the entire cell after the test. The perforated cell was still capable of lighting a light bulb, as shown in Figure 10d.

2.6. Electrochemical Performance

The electrolyte wettability of the separator plays a crucial role in the performance of LIBs because it not only affects the manufacturing process but also significantly impacts the ionic transport between electrodes.[14,22] However, the separators widely used are based on polyolefin materials that have poor electrolyte wettability because of their polarity incompatibility with the liquid electrolyte. The contact angles of the PE separator, APPCS, and APP-CCS@PFR were measured to evaluate the electrolyte wettability, and the results are shown in Figure S11a–c (Supporting Information). The PE separator exhibited poor electrolyte wettability with a large contact angle of 66.6°. After the modification of APP, the contact angles of both AAPCS and APP-CCS@PFR decreased markedly to near zero. The results indicated that APPCS and APP-CCS@PFR had better electrolyte wettability than the PE separator, which was because of the porous structure of the APP-coated layer and the good affinity of APP to the electrolyte.

Table 1. The electrolyte uptake and ionic conductivity of the PE separator, APPCSC, and APP-CCS@PFR.

Separator	PE	APPCS	APP-CCS@PFR
Thickness [µm]	20	25	28
Gurley value [s 100 mL^{-1}]	215.8	234.3	249.6
Electrolyte uptake [%]	56	69	73
Ion conductivity [mS cm^{-1}]	0.54	0.62	0.65

Table 1 presents the physical properties of the PE separator, APPCS, and APP-CCS@PFR. The Gurley value was tested by recording the time taken for 100 mL of air to penetrate through the separator. After the coating of APP and the Al_2O_3 ceramic particles, the Gurley value of APPCS and APP-CCS@PFR slightly increased to 234.3 s and 249.6 s 100 mL^{-1}, respectively, as compared to the 215.8 s 100 mL^{-1} for the PE separator. Despite this, the modifications of APP and the Al_2O_3 ceramic particles had little negative impact on the electrochemical performance of the LIBs because of the improved electrolyte wettability. Owing to the poor wettability, the PE separator showed a low electrolyte uptake of 56%. In contrast, APPCS and APP-CCS@PFR had a higher electrolyte uptake of 69% and 73%, respectively. This is because the liquid electrolyte could not only be captured in the micropores of the PE separator but could also be absorbed on the affiliative surfaces and inside the pores of both the APP-coated layer and the ceramic-coated layer. The greater the amount of liquid electrolyte absorbed in the membrane, the higher the ionic conductivity will be. As expected, APPCS and APP-CCS@PFR had a higher ionic conductivity at room temperature of 0.62 and 0.65 mS cm^{-1}, respectively, as compared to the PE separator at 0.54 mS cm^{-1}, as calculated by the electrochemical impedance spectrum shown in Figure S12 (Supporting Information).

The cycle performance of the cell assembled with APP-CCS@PFR was evaluated by $LiNi_{0.8}Co_{0.1}Mn_{0.1}O_2|SiO_x$-Gr full cells at 0.5 C (1.8 mA cm^{-2}) and a commercial PE separator was used as a control. **Figure 11**a shows that the capacity retention after 100 cycles of the cell assembled with APP-CCS@PFR was 90.7%, which was close to the 90.2% capacity retention shown by the cell assembled with the commercial PE separator. Both types of cells maintained a high Coulombic efficiency above 99.8%. Figure 11b depicts the discharge curves of the cell at various cycles. The discharge curves of the cell assembled with APP-CCS@PFR were similar to those of the cell assembled with the PE separator. Therefore, the cycle performance demonstrated that the modification of APP had no negative influence on the electrochemical performance of the battery.

3. Conclusions

In summary, a rational design for a high-safety battery assembled with a heatproof–fireproof bifunctional separator was

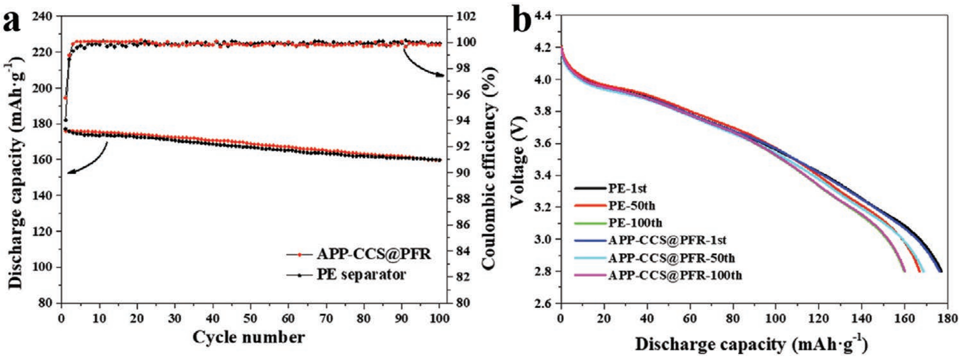

Figure 11. a) Cyclic performance of $LiNi_{0.8}Co_{0.1}Mn_{0.1}O_2|SiO_x$-Gr full cells assembled with a PE separator and APP-CCS@PFR and b) their discharge curves.

developed by coating APP particles on the surface of CCS@PFR. The CCS@PFR substrate separator had an excellent thermal stability without visible shrinkage at 300 °C, which prevented the internal short-circuit of the battery and simultaneously provided a thermally dimensional stable supporting layer for the APP-coated layer. The APP-coated layer decomposed into NH_3, H_2O, and PPA at high temperatures. NH_3 and H_2O suppressed combustion by diluting the concentration of combustible gas and oxygen to some extent. PPA formed a dense overall-covered layer on both the surfaces of the cathodes and batteries preventing contact between the combustibles and the oxidants, including oxygen in the air and the highly reactive oxygen released from the cathode at high temperatures. Simultaneously, PPA further carbonized combustibles into nonflammable char residues, which converted violent and rapid combustion reactions into mild and stepwise exothermic reactions. The consequent carbonized layer acted as an obstruction layer to further restrain the transfer of heat, combustible gas, and oxygen. Consequently, $LiNi_{0.8}Co_{0.1}Mn_{0.1}O_2|SiO_x$-Gr full cells assembled with APP-CCS@PFR showed an excellent safety performance without catching fire during a 30 s combustion test and 10 min high-temperature test above 300 °C. Additionally, 3 Ah $LiNi_{0.8}Co_{0.1}Mn_{0.1}O_2|SiO_x$-Gr full cells assembled with APP-CCS@PFR successfully passed the ARC and nail penetration tests without a violent thermal runaway.

Our strategy suggests that the safety performance of LIBs will be effectively improved if the fire triangle is broken by restraining the diffusion of oxygen, heat, and combustible gas. A physical-isolation flame retardant that can form a dense incombustible isolated layer at elevated temperatures would be feasible. Additionally, it also effectively enhanced the safety of the LIBs by converting the combustibles into nonflammable intermediate products and by converting intense combustion reactions into mild stepwise exothermic reactions. Such a novel strategy can also be extended to other systems, providing a new perspective to improve the safety performance of LIBs.

4. Experimental Section

Preparation of the Pulverized APP Particles: Pristine commercial APP particles ($n > 1000$, supplied by China Aviation Lithium Battery Co., Ltd., China) were pulverized by mechanical ball milling at various rates for 10 h with 1 mm zirconia beads in a zirconia ball mill jar (beads:APP = 20:1, by weight). The pulverized APP particles were then dispersed in deionized water and collected by centrifugation at a rate between 1000 and 8000 r min^{-1}. After drying in a vacuum oven at 70 °C for 24 h, the pulverized APP was stored in a desiccator for subsequent use.

Preparation of APP-CCS@PFR: CCS@PFR was prepared as described in a previous study.[10] A single-sided ceramic-coated separator, with a 3 µm Al_2O_3 coating layer on a 20 µm PE separator (Jinhuigaoke, Guangdong, China), was immersed in a 50 g L^{-1} PFR (Mw ≈ 2000, Shanghai Macklin Biochemical Co., Ltd., China) solution with ethanol as the solvent. After removing the redundant solution, the separator was placed in a vacuum oven at 70 °C for 24 h, and CCS@PFR was obtained. The slurry for the APP coating layer was prepared by mixing 0.95 g pulverized APP particles, 0.02 g carboxymethyl cellulose, and 0.03 g styrene butadiene rubber into a hybrid solvent of water and ethanol (V:V = 1:1). After 10 min of ultrasonic dispersion and 24 h of vigorous stirring, the slurry was coated onto the ceramic uncoated side of the CCS@PFR using an automatic film coating machine (Shanghai Environmental Engineering Technology Co., Ltd., China) at a speed of 2.5 cm s^{-1}. The slit of the applicator was 120 µm with an adjustable coating rod. APP-CCS@PFR was obtained after removing the solvent at 60 °C for 24 h under a vacuum atmosphere. Additionally, pulverized APPCS was prepared as a control separator by the same process.

Electrode Preparation and Cell Assembly: The cathode pole piece contains 97.75 wt% $LiNi_{0.8}Co_{0.1}Mn_{0.1}O_2$ active material, 0.75 wt% CNTs, 1 wt% PVDF, and 0.5 wt% Super P. Moreover, the positive material load was ≈20 mg cm^{-2}. The anode pole piece (SiO_x-Gr) consists of 84.92 wt% graphite, 10.5 wt% SiO_x, 1.00 wt% conductive agent, and 3.58 wt% composite binder. Both the cathode and anode pole pieces were provided by Tianjin JEVE Power Co., Ltd., with the capacity ratio of negative electrode:positive electrode = 1.13:1. The battery performances were tested using 2016 coin cells by sandwiching separators between the anodes and cathodes with 90 µL commercial LB301 electrolyte (containing 1 mol L^{-1} $LiPF_6$ dissolved in a hybrid solvent of ethylene carbonate and dimethyl carbonate, V:V = 1:1, Zhangjiagang Guotaihuarong New Chemical Materials Co., Ltd., China). All cells were assembled in a glove box (M. Braun GmbH, Germany) under an argon atmosphere.

The batteries for the combustion and high-temperature tests were assembled through a winding process by wrapping the electrodes inside the separator with 600 µL of commercial LB301 electrolyte. The 3 Ah pouch cells for the nail penetration and ARC tests were assembled through a stacking process. The cells were stacked in the order of separator, anode, separator, cathode, separator, anode, separator, and so on by facing the fireproof layer of APP-CCS@PFR to the cathode. The electrode pieces were double-side-coated. Then, the nickel and aluminum pole ears were welded to the anodes and cathodes, respectively, using a point welding machine. Subsequently, an aluminum-plastic film was applied by a heat sealing machine to package it (Jiqiang Automation Equipment Co., Ltd., China) while maintaining an opening to inject the electrolyte. The package was then dried in an 80 °C vacuum oven for 24 h. After injecting 15 mL of commercial LB301 electrolyte and heat-sealing in a glove box under an argon atmosphere, the batteries were charged to 4.3 V for testing.

Characterization and Measurements: The surface and cross-sectional morphologies of the APP particles and APP-CCS@PFR were investigated using field-emission scanning electron microscopy (FESEM, S-4800, Hitachi, Japan). The cross-sectional samples of the separators prepared for SEM were mechanically broken after being cooled in liquid nitrogen. A Leica EM TIC 3X (Leica Microsystems, Wetzlar, Germany) was used to prepare cross-sectional samples of the cathode after high-temperature testing. The size distribution of APP particles was evaluated using a Marvin laser granulometer (MS2000, England). The transmitted infrared spectrum and attenuated total reflection infrared spectrum were analyzed using FTIR spectroscopy (Nicolet IS5 spectrometer, Thermo Fisher Scientific Inc., America) in the range of 400–4000 and 600–4000 $\mathrm{cm^{-1}}$, respectively. DSC and TGA analyses were conducted using a Model STA 449 instrument (NETZSCH Machinery and Instruments Co., Ltd.) at a heating rate of 5 °C $\mathrm{min^{-1}}$ from 35 to 800 °C in a nitrogen or purified air atmosphere. The Gurley value was tested with Genuine Gurley4320 by recording the time it took for 100 mL of air to penetrate through the separator.

The thermal shrinkage of the separators was tested by measuring the dimensional change after being subjected to heat treatment at various temperatures for 30 min. The thermal shrinkage (T_s) of the separators can be computed according to the following equation

$$T_s = \frac{S_0 - S}{S_0} \times 100\% \qquad (1)$$

where S_0 and S are the areas of the separators before and after heat treatment, respectively. The electrolyte uptake of the separators was obtained with a commercial LB301 electrolyte according to the following equation

$$\mathrm{Eu} = \frac{W - W_0}{W_0} \times 100\% \qquad (2)$$

where W_0 and W are the original weight of the separators and the weight of the separators with full liquid electrolyte absorption, respectively. The ionic conductivity of the separator was measured using a blocking-type cell by sandwiching a separator between two stainless steel sheets. An adequate amount of electrolyte was injected into the cell to wet the separator, and the impedance data was recorded by an electrochemical working station (AutoLab, Sino-Metrohm Technology, Ltd., China) in the frequency range of 1 Hz to 100 kHz with a perturbation voltage of 10 mV. The ionic conductivity (σ) was computed by the following equation

$$\sigma = \frac{d}{R_b \times A} \qquad (3)$$

where R_b is the bulk impedance of the separator by fitting the result of AC impedance, d is the thickness of the separator obtained by the screw micrometer, and A represents the area of the stainless steel sheets. To investigate the wettability of the separator to the electrolyte, contact angle tests of the PE separator, APPCS, and APP-CCS@PFR were conducted using a commercial drop shape analysis system (Powereach JC2000C1, Shanghai Zhongchen Digital Technique Equipment Co. Ltd., China).

The nail penetration test was conducted using a battery nail penetration tester (Guangdong Dongguan Beier Testing Equipment Co. Ltd., China) with a 3 mm diameter stainless steel nail at a rate of 1 cm $\mathrm{s^{-1}}$. ARC (Hazard Evaluation Laboratory Co. Ltd., England) was used to evaluate the safety performance of the batteries by heating 5 °C per step with a detection limit of 0.03 °C $\mathrm{min^{-1}}$ under adiabatic conditions. The cycle performances of the cells assembled with the PE separator and APP-CCS@PFR were measured using a battery testing system (LAND-V34, Wuhan LAND Electronics Co., Ltd., China) at a constant current rate of 0.5 C under the voltage range of 2.8–4.3 V.

Supporting Information

Supporting Information is available from the Wiley Online Library or from the author.

Acknowledgements

The authors gratefully acknowledge the financial support from the National Natural Science Foundation of China (21875198, 21875195), National Key Research and Development Program of China (2017YFB0102000), Fundamental Research Funds for the Central Universities (20720190040), and The Key Project of Science and Technology of Fujian Province (2018H6019).

Conflict of Interest

The authors declare no conflict of interest.

Keywords

ceramic-coated separator, high energy density, high safety, inflaming retarding, lithium-ion battery

Received: October 7, 2020
Revised: November 18, 2020

---

[1] a) J. M. Tarascon, M. Armand, *Nature* **2001**, *414*, 359; b) M. M. Thackeray, C. Wolverton, E. D. Isaacs, *Energy Environ. Sci.* **2012**, *5*, 7854; c) B. Scrosati, J. Hassoun, Y.-K. Sun, *Energy Environ. Sci.* **2011**, *4*, 3287.

[2] a) M. Chi, L. Shi, Z. Wang, J. Zhu, X. Mao, Y. Zhao, M. Zhang, L. Sun, S. Yuan, *Nano Energy* **2016**, *28*, 1; b) X. N. Feng, D. S. Ren, X. M. He, M. G. Ouyang, *Joule* **2020**, *4*, 743; c) H. Lee, M. Yanilmaz, O. Toprakci, K. Fu, X. Zhang, *Energy Environ. Sci.* **2014**, *7*, 3857.

[3] a) J. Dai, C. Shi, C. Li, X. Shen, L. Peng, D. Wu, D. Sun, P. Zhang, J. Zhao, *Energy Environ. Sci.* **2016**, *9*, 3252; b) K. M. Diederichsen, E. J. McShane, B. D. McCloskey, *ACS Energy Lett.* **2017**, *2*, 2563.

[4] a) H. U. Escobar-Hernandez, R. M. Gustafson, M. I. Papadaki, S. Sachdeva, M. S. Mannan, *J. Electrochem. Soc.* **2016**, *163*, A2691; b) C. Liu, H. Li, X. Kong, J. Zhao, *Int. J. Heat Mass Transfer* **2020**, *153*, 119590; c) H. Li, C. Liu, X. Kong, J. Cheng, J. Zhao, *J. Power Sources* **2019**, *438*, 226971; d) H. Li, X. Kong, C. Liu, J. Zhao, *Appl. Therm. Eng.* **2019**, *161*, 114144.

[5] a) P. Shi, H. Zheng, X. Liang, Y. Sun, S. Cheng, C. Chen, H. Xiang, *Chem. Commun.* **2018**, *54*, 4453; b) D. G. Belov, D. T. Shieh, *J. Power Sources* **2014**, *247*, 865.

[6] a) Y. Ding, X. Shen, J. Zeng, X. Wang, L. Peng, P. Zhang, J. Zhao, *Solid State Ionics* **2018**, *323*, 16; b) P.-Y. Ji, J. Fang, Y.-Y. Zhang, P. Zhang, J.-B. Zhao, *ChemElectroChem* **2017**, *4*, 2352; c) Y. Chen, L. Li, L. Xu, L. Qian, *J. Appl. Polym. Sci.* **2018**, *135*, 46334; d) W. Zhang, J. Nie, F. Li, Z. L. Wang, C. Sun, *Nano Energy* **2018**, *45*, 413; e) Y. Liu, C. Li, B. Li, H. Song, Z. Cheng, M. Chen, P. He, H. Zhou, *Adv. Energy Mater.* **2018**, 1702374; f) M. Martinez-Ibañez, E. Sanchez-Diez, L. Qiao, Y. Zhang, X. Judez, A. Santiago, I. Aldalur,

J. Carrasco, H. Zhu, M. Forsyth, M. Armand, H. Zhang, *Adv. Funct. Mater.* **2020**, *30*, 2000455; g) H. W. Kim, J. Han, Y. J. Lim, Y. Choi, E. Lee, Y. Kim, *Adv. Funct. Mater.* **2020**, https://doi.org/10.1002/adfm.202002008.

[7] a) D. Ren, X. Liu, X. Feng, L. Lu, M. Ouyang, J. Li, X. He, *Appl. Energy* **2018**, *228*, 633; b) X. Liu, D. S. Ren, H. J. Hsu, X. N. Feng, G. L. Xu, M. H. Zhuang, H. Gao, L. G. Lu, X. B. Han, Z. Y. Chu, J. Q. Li, X. M. He, K. Amine, M. G. Ouyang, *Joule* **2018**, *2*, 2047.

[8] a) L. Xia, *J. Anal. Appl. Pyrolysis* **2018**, *134*, 265; b) F. Xin, C. Zhai, C. Guo, Y. Chen, L. Qian, X. Chen, *J. Polym. Res.* **2018**, *25*; c) S. Yu, H. Xiang, J. Zhou, M. Zhu, *Prog. Nat. Sci.: Mater. Int.* **2018**, *8*; d) Y.-Q. Shi, T. Fu, Y.-J. Xu, D.-F. Li, X.-L. Wang, Y.-Z. Wang, *Chem. Eng. J.* **2018**, *354*, 208.

[9] a) X. Liu, X. Jiang, Z. Zeng, X. Ai, H. Yang, F. Zhong, Y. Xia, Y. Cao, *ACS Appl. Mater. Interfaces* **2018**, *10*, 38141; b) Z. Zeng, V. Murugesan, K. S. Han, X. Jiang, Y. Cao, L. Xiao, X. Ai, H. Yang, J.-G. Zhang, M. L. Sushko, J. Liu, *Nat. Energy* **2018**, *3*, 674.

[10] L. Peng, X. Shen, J. Dai, X. Wang, J. Zeng, B. Huang, H. Li, P. Zhang, J. Zhao, *J. Electrochem. Soc.* **2019**, *166*, A2111.

[11] a) W. Fu, R. Xu, X. Zhang, Z. Tian, H. Huang, J. Xie, C. Lei, *J. Power Sources* **2019**, *436*, 226839; b) S. Gong, H. Jeon, H. Lee, M. H. Ryou, Y. M. Lee, *ACS Appl. Mater. Interfaces* **2017**, *9*, 17814.

[12] a) Z.-B. Shao, C. Deng, Y. Tan, L. Yu, M.-J. Chen, L. Chen, Y.-Z. Wang, *J. Mater. Chem. A* **2014**, *2*, 13955; b) G. Camino, L. Costa, L. Trossarelli, *Polym. Degrad. Stab.* **1985**, *12*, 16.

[13] a) H. Li, D. Wu, J. Wu, L. Y. Dong, Y. J. Zhu, X. Hu, *Adv. Mater.* **2017**, *29*, 1703548; b) D. Li, D. Shi, Z. Yuan, K. Feng, H. Zhang, X. Li, *J. Membr. Sci.* **2017**, *542*, 1; c) C. Shi, P. Zhang, L. Chen, P. Yang, J. Zhao, *J. Power Sources* **2014**, *270*, 547; d) C. Shi, P. Zhang, S. Huang, X. He, P. Yang, D. Wu, D. Sun, J. Zhao, *J. Power Sources* **2015**, *298*, 158.

[14] C. Shi, J. Dai, C. Li, X. Shen, L. Peng, P. Zhang, D. Wu, D. Sun, J. Zhao, *Polymers* **2017**, *9*, 159.

[15] J. W. Lee, A. M. Soomro, M. Waqas, M. A. U. Khalid, K. H. Choi, *Int. J. Energy Res.* **2020**, *44*, 7035.

[16] a) Y. X. Wei, C. Deng, H. Chen, L. Wan, W. C. Wei, Y. Z. Wang, *ACS Appl. Mater. Interfaces* **2018**, *10*, 28036; b) W. Liu, D.-Q. Chen, Y.-Z. Wang, D.-Y. Wang, M.-H. Qu, *Polym. Degrad. Stab.* **2007**, *92*, 1046; c) S. Bourbigot, M. Le Bras, R. Delobel, *Carbon* **1995**, *33*, 10.

[17] M. S. Gonzalez, Q. Yan, J. Holoubek, Z. Wu, H. Zhou, N. Patterson, V. Petrova, H. Liu, P. Liu, *Adv. Mater.* **2020**, *32*, 1906836.

[18] a) T. Zhang, H. Yan, M. Peng, L. Wang, H. Ding, Z. Fang, *Nanoscale* **2013**, *5*, 3013; b) Z. B. Shao, C. Deng, Y. Tan, M. J. Chen, L. Chen, Y. Z. Wang, *ACS Appl. Mater. Interfaces* **2014**, *6*, 7363.

[19] X. Kong, J. Liu, Y. Zhang, J. Zeng, J. Zhao, *Electrochim. Acta* **2020**, *349*, 136356.

[20] Z. Liu, Q. Yu, Y. Zhao, R. He, M. Xu, S. Feng, S. Li, L. Zhou, L. Mai, *Chem. Soc. Rev.* **2019**, *48*, 285.

[21] L.-P. Dong, S.-C. Huang, Y.-M. Li, C. Deng, Y.-Z. Wang, *Ind. Eng. Chem. Res.* **2016**, *55*, 7132.

[22] a) F. Jiang, Y. Nie, L. Yin, Y. Feng, Q. Yu, C. Zhong, *J. Membr. Sci.* **2016**, *510*, 1; b) C. Shi, J. Dai, S. Huang, C. Li, X. Shen, P. Zhang, D. Wu, D. Sun, J. Zhao, *J. Membr. Sci.* **2016**, *518*, 168.